Colloids and Surfaces A 558 (2018) 8–15

Contents lists available at ScienceDirect

Colloids and Surfaces A

journal homepage: www.elsevier.com/locate/colsurfa

In-situ analysis of nucleation and growth of transition metal oxalate battery precursor particles via time evolution of solution composition and particle size distribution

Hongxu Dong[a], Anny Wang[a], Guillermo Smart[b], Dave Johnson[c], Gary M. Koenig Jr.[a,*]

[a] Department of Chemical Engineering, University of Virginia, 102 Engineers Way, Charlottesville, VA, 22904-4741, USA
[b] Mettler Toledo Autochem, 6708 Alexander Bell Drive, Columbia, MD, 21046, USA
[c] Advanced TechniSales, 17929 Kings Point Drive, Cornelius, NC, 28031, USA

GRAPHICAL ABSTRACT

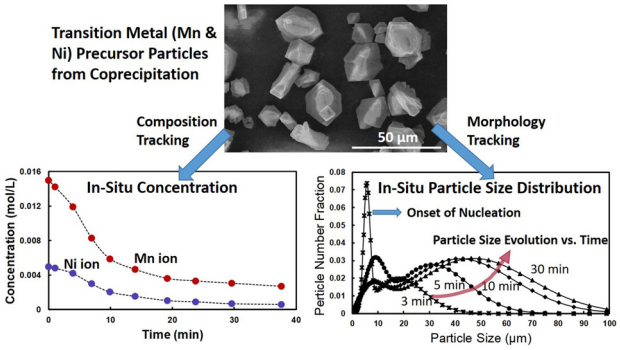

ARTICLE INFO

Keywords:
Coprecipitation
Nucleation
Particle growth
FBRM
Lithium-ion batteries
Cathode materials

ABSTRACT

Precise control over particle composition and morphology is essential for the optimization of electroactive, multi-component transition metal oxides used as lithium-ion battery cathode materials. These transition metal oxide particles are often synthesized using precursors produced via coprecipitation reactions, in part due to the advantages provided by coprecipitation including scalability and homogeneous mixing of different transition metal ions. Understanding the kinetics of the nucleation and particle growth for each individual transition metal within a multicomponent blend solution is critical for rational and explicit control of particle composition, as well as to dictate the particle morphology. In this study, in-situ particle size distribution was measured during coprecipitation reactions using focused beam reflection. The transition metal concentrations were also in-situ tracked during the process which, in combination with the particle size information, provided detailed information on the reaction rate, reaction order, and mechanisms of particle nucleation and growth. This work is the first demonstration of application of such techniques to battery precursor particle synthesis, and provides insights into important observations during the coprecipitation process such as the change in the rate of coprecipitation of different transition metals when reacted in isolation or in a blend with other components. The techniques and analysis demonstrated in this paper could find application across many multicomponent transition metal coprecipitation systems important to various applications, including energy storage materials.

* Corresponding author.
E-mail addresses: hd5cw@virginia.edu (H. Dong), aw5nc@virginia.edu (A. Wang), Guillermo.Smart@mt.com (G. Smart), djohnson@advancedtechnisales.com (D. Johnson), gary.koenig@virginia.edu (G.M. Koenig).

https://doi.org/10.1016/j.colsurfa.2018.08.047
Received 21 June 2018; Received in revised form 17 August 2018; Accepted 18 August 2018
Available online 20 August 2018

1. Introduction

Lithium-ion (Li-ion) batteries have become a successful energy storage technology due to their high energy density and capability to meet a variety of power and energy requirements for a wide diversity of applications [1,2]. The flexibility of Li-ion battery functionality results from the variety of battery active material options, and for the cathode, particles comprised of multicomponent transition metal (TM) oxides are currently the most commonly used [3,4]. To successfully design or choose a particular multicomponent TM oxide cathode material, careful control is needed over the chemical composition of the material because the material structure and electrochemical properties are highly sensitive to the TM composition, and even slight deviations in stoichiometry can significantly influence battery performance [5–9]. Coprecipitation is a popular route to synthesize the precursors used for TM oxide battery particles due to the homogeneous mixing of different TMs at the atomic level that is achieved with this method [5,10–19]. The obtained precursor materials are then converted to the final battery active materials via high temperature calcination processes. However, although achieving the appropriate TM composition and distribution during the initial coprecipitation synthesis process is critical for rational control over electrochemical properties of battery materials, little has been reported on the details of the coprecipitation solution chemistry using multiple TM cations. While often the TM composition of the precursor particles is assumed to reflect the stoichiometry of the dissolved TM feed to the process, under some solution conditions this assumption is not appropriate and can result in measurable deviations of the expected properties of the battery active material after calcination [5].

Recently a technique was described in the literature to track the TM composition as a function of time during the coprecipitation process, and the method was applied for pure precipitates containing one TM and multicomponent precipitates where each individual TM was tracked independently [5]. This technique used inductively coupled plasma optical emission spectroscopy (ICP-OES) to analyze the compositions of the solid and solution phase separately at multiple collection times during batch reactor coprecipitation. While this technique gives important insights into precipitate composition as a function of time, it cannot determine the normalized (by solid phase surface area) rate of TM precipitation onto the solid phase and cannot differentiate between particle nucleation and particle growth during the process because there was not information simultaneously collected on the particle size distribution (PSD). To obtain insights into these processes, the PSD must be collected in-situ during the coprecipitation process and combined with the compositional information. PSD measurements via image analysis (including both optical and electron microscopies) have been used previously in crystallization phenomena studies [20–23]. While these methods have been successfully applied to many systems, it is challenging to image the particles directly in the batch reactor in-situ, and ex-situ observation has a lag time in transferring and/or preparing samples that will modify the solution chemistry relative to the simultaneously collected compositional information. Thus, a technique was needed to provide in-situ information during the coprecipitation process of the PSD with temporal resolution equal to or better than the compositional information. For the study described herein, the technique that was employed to obtain the in-situ PSD information was Focused Beam Reflectance Measurement (FBRM) [24–29]. FBRM operates using a probe that is directly inserted into the reaction solution. The probe has a laser which is focused in a focal plane beyond a sapphire window at the end of the cylindrical probe. The laser rotates at a high fixed speed and as the beam crosses over particles within the focal plane the laser beam intersects the edge of the particle and the laser light is backscattered. The backscattered light is transmitted back up the probe to the detector, and the backscattered signal continues until the beam has gone beyond the other side of the particle surface. Thus, the backscattered light is transmitted as it traverses the particle from edge to edge, and because the laser is scanned with a fixed speed, the edge-to-edge time scale is converted to a length scale which is known as the chord length. The laser passes over many particles as it sweeps, and thus a chord length distribution (CLD) is obtained from the FBRM analysis. The PSD rather than the CLD was desired for the analysis in this study, and the CLD was converted to a PSD using methods previously reported which will be discussed in further detail in the Experimental section [30]. The FBRM technique is fast and can produce large statistics on the particle populations as long as the number of particles in the suspension is sufficient.

In this study, we tracked the in-situ PSD of TM oxalate precipitates using FBRM, and combined this information with the precipitation rate of the TMs obtained from compositional analysis of the reaction solution as a function of time. With these combined techniques, the rate of precipitation normalized to the surface area of the precipitate was obtained. Such information is necessary to rationally control the synthesis of multicomponent TM precipitates, and this is the first report of applying such analysis to battery precursor particles. In addition, the in-situ tracking of the PSD during precipitation provided insights into the nucleation and growth processes of these precipitate materials. The model system chosen was oxalate precipitation with pure and mixed solutions of manganese and nickel, an important system towards precursor synthesis for multiple battery active materials, such as $LiMn_{1.5}Ni_{0.5}O_4$, $LiMn_{0.5}Ni_{0.5}O_2$, and $LiNi_{1/3}Mn_{1/3}Co_{1/3}O_2$ [5,31,32]. In particular, a 3:1 Mn:Ni feed ratio was chosen because this precipitate stoichiometry is necessary for precursors used to form high purity $LiMn_{1.5}Ni_{0.5}O_4$, which is a promising high voltage cathode material [33,34]. Oxalate precipitation was chosen because both nickel and manganese (and other TM of interest to battery precursors including cobalt) form stable oxalate dihydrate particles, whereas other popular battery precursor particle precipitate systems such as hydroxides or carbonates have the additional complexity of the simultaneous formation of multiple types of precipitates or the oxidation of the precipitate while still in solution [35,36].

2. Experimental

2.1. Coprecipitation synthesis

The coprecipitation synthesis was adapted from previous work [5]. In brief, the TM solution and oxalate solution were prepared separately by dissolving laboratory grade $MnSO_4{\cdot}H_2O$ and $NiSO_4{\cdot}6H_2O$ for the TM solution and $Na_2C_2O_4$ for the oxalate solution in deionized water (DI) heated to 60 °C (all reagents from Fisher). The two solutions were mixed by pouring the TM solution all at once into the oxalate solution. The concentrations of total TM ions, and oxalate, in the mixed solution were predetermined and were set at 20 mM at the initiation of all precipitation experiments. In the manganese and nickel blend coprecipitation, the TM solution contained manganese and nickel with 3:1 ratio, while the total TM concentration was still the same as oxalate. The fast pouring, as well as a magnetic stir bar spinning at 300 rpm, provided mixing to ensure a homogeneous solution. In addition to preheating to 60 °C before mixing, during the reaction the temperature was kept at 60 °C and the stir bar was maintained at 300 rpm. Syringes were used with syringe filters to collect the solute during periodic time intervals over the course of the reaction for compositional analysis. For solution compositional analysis, a sample (~2 mL) was withdrawn from the 1 L beaker reaction vessel using a 3 mL syringe. For the withdrawn sample, the aqueous phase was quickly separated from the solid precipitate particles by forcing the solution through a 33 mm diameter syringe filter with 0.22 mm pore size (Fisherbrand). The aqueous phase was further digested using aqua regia and diluted with DI water into a proper concentration for ICP-OES analysis (PerkinElmer Optima 8000), which was 0.1 to 10 ppm.

2.2. Characterization of particle size and shape

During the coprecipitation reaction, a ParticleTrack G400 (Mettler Toledo) with FBRM capability was used for in-situ determination of the PSD throughout the coprecipitation reaction by immersing the FBRM probe directly into the reaction environment. The probe was inserted into the solution such that the laser window was located roughly at the center of the beaker reactor. The CLD averaged over a 10 s interval was collected throughout an experiment until negligible changes in either particle counts or CLD was observed. At the conclusion of one hour of the coprecipitation reaction proceeding, the particle shapes and sizes were also characterized using a scanning electron microscope (SEM, FEI Quanta 650) after filtering and complete drying. Thermal gravimetric analysis (TGA, TA Q50) was performed to determine the water stoichiometry of the precipitates. TGA analysis for all the precipitate particles synthesized for this study confirmed two structural water for each transition metal oxalate unit (e.g., dihydrates).

2.3. Conversion from CLD to PSD and normalization of reaction rates

In the conversion from the directly measured CLD with the FBRM to a PSD, an essential assumption was made that the number of particles analyzed was large enough that the probability of measuring a chord within a particular size range was equated to the fraction of the total number of particles which would be measured as having the chord length within this size range. It is expected that the number of particles recorded by the FBRM was high enough that this assumption was valid [30]. The conversion from CLD to PSD was completed using the method described by Pandit at al. [30]. First, an initial guess was made for the mean and the variance of a normal distribution function that expressed a PSD. The number of independent normal distributions used in the fitting were dependent on the number of independent peaks in the CLD that were observed for each scan (e.g.; 1 normal distribution was fit for a single peak while 3 normal distributions were used for 3 peaks). Next, the discrete PSD was formed using the guessed normal distribution and converted to a discrete CLD with bin sizes the same as those of the CLD data. The two parameters for each normal distribution were adjusted using the least squares method to minimize the difference between the CLD from the FBRM experimental measurements and the calculated CLD using the fitted PSDs. The R^2 values for the calculated compared to the measured CLDs were no less than 0.97, indicating good fits of the measured CLDs using the PSD parameters.

3. Results and discussion

Measuring the concentrations of the TM remaining in solution at different time points during the coprecipitation was necessary to determine the reaction rates associated with the formation of the particle precipitates. The TM concentrations remaining in solution was determined during the precipitation with initial TM feeds of pure nickel, pure manganese, and a “blend” system (with the TM feed ratio being 3:1 Mn:Ni). The results for the three systems are in shown in Fig. 1. The pure manganese oxalate ($MnC_2O_4{\cdot}2H_2O$, referred to as MnOx) coprecipitation proceeds quickly over the first ten minutes and plateaus after roughly 20 min. On the contrary, the pure nickel oxalate ($NiC_2O_4{\cdot}2H_2O$, referred to as NiOx) coprecipitation consumes the TM ion at a lower initial rate, and the residual Ni solution concentration does not reach a plateau until after an hour. In the blend system (Mn:Ni feed ratio 3:1, with the precipitate concentration slightly changing with reaction time and reaching $Mn_{0.72}Ni_{0.28}C_2O_4{\cdot}2H_2O$ at the one hour collection time, referred to as Mn3Ni1Ox), the reaction proceeds in a manner qualitatively more similar to the pure manganese reaction, and this system will be discussed in further detail later.

Fig. 2 shows the total chord counts from the FBRM probe as a function of the time after initiating the coprecipitation for the NiOx, MnOx, and the Mn3Ni1Ox reaction systems. A linear relationship has previously been reported between the particle density and FBRM particle count for suspensions that contain particles of similar and larger

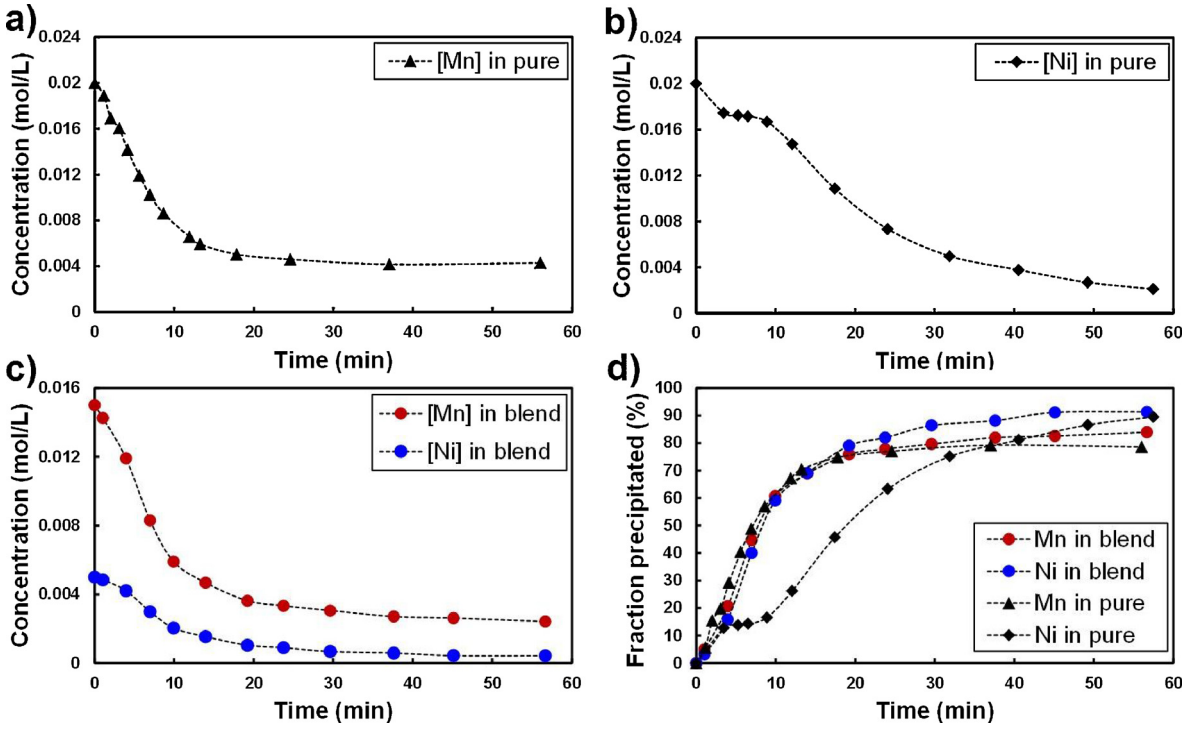

Fig. 1. Residual soluble (a) Mn (triangles) and (b) Ni (diamonds) in solution during coprecipitation of pure manganese oxalate and pure nickel oxalate. (c) Residual soluble Mn (blue circles) and Ni (red circles) during coprecipitation of feed with 3:1 Mn:Ni ratio. The total concentrations of TM and oxalate at the beginning of the coprecipitation for all solutions were 20 mM. (d) Fraction of Mn and Ni ions in precipitate phase. Dashed lines added to guide the eye. (For interpretation of the references to colour in this figure legend, the reader is referred to the web version of this article.)

sizes than the particles in this study [27]. This linear relationship has been reported to hold until the FBRM particle count reaches as high as 10,000. The inset in Fig. 2 is the enlarged view of the first 10 min of the reaction. From this enlarged view it can be found that particles begin to form after around 1 min for the pure manganese system, 4.5 min for the pure nickel system, and 1.5 min for the blend system. Note that the limit of detection for the FBRM is 0.5 μm, thus this onset is the point where particles of at least this size were measured in the solution. These onset times were consistent with rough observations of the induction times, with the induction time being the time for the initial clear solutions to become cloudy to the naked eye. From the dissolved TM concentration vs. time plots (Fig. 1) it was observed that NiOx coprecipitation had a relatively slower transition period for Ni going to the particle phase after the solutions were mixed. The time lag observed for detecting particles with the FBRM, slower detected loss of Ni from the solution phase, and longer induction times observed implied that NiOx crystallization from the solution has a slower nucleation rate. After the increase in FBRM particle counts at ~4.5 min for the NiOx system the particle count continuously increased out to even 50 min after the solutions were mixed. Even though the particle counts passed the 10,000 upper limit to meet the linear relationship between the count and particle density after 10 min, the increase in particle counts still reflected the continuous particle formation in the solution. In contrast, MnOx and Mn3Ni1Ox systems have their FBRM counts plateau much more quickly, after 3 min and 10 min respectively. Continuous particle formation rather than particle growth by solute depositing on existing particles may explain the lower rate of loss of the soluble Ni species in the NiOx reaction even after the induction period. The pure Mn precipitation; however, had relatively rapid particle formation (marked by the short period of increase in FBRM counts and stable plateau in Fig. 1) followed closely by particle growth. Particle growth has previously been reported to be a lower energy barrier relative to nucleation [37], and thus this interpretation was consistent with the faster consumption of soluble Mn during MnOx precipitation. For the Mn3Ni1Ox coprecipitation system, there was relatively fast particle formation and a plateau in the FBRM counts similar to the observations for MnOx system, although the timescale for a plateau in the counts was longer than for MnOx system. We suspect the longer time to reach a plateau in particle counts for the Mn3Ni1Ox system was due to the continuous formation of NiOx crystals, as supported by the FBRM data (Fig. 2). In our earlier work [5], we also observed an increased reaction rate of nickel ions to the precipitate phase in the blend system. It was speculated that the fast crystallization of the MnOx particles provided seeds for the nickel ions to deposit onto and thus to grow faster. Previous literature on nucleation and particle growth has reported the precipitation rate to be a linear function of the suspension density for several inorganic salts [29]. While suspension density and particle seeding heavily influence precipitation rate during the early nucleation stage, other factors including surface roughness have a great effect on precipitation rate during the later particle growth stage. The potential influence of surface roughness will be described in further detail for the oxalate particles later in the discussion.

The 10-second averaged CLD as a function of reaction time for all three systems were obtained using the FBRM probe and converted to PSDs using the method described in the Experimental section. It is noted that the CLD was not square weighted such that information could be extracted at earlier times when only smaller particles were formed. The resulting PSDs from the FBRM measurements at 5, 10, and 30 min after the start of the coprecipitation reactions for each of the three systems are shown in Fig. 3. For the two faster precipitating systems, MnOx and Mn3Ni1Ox, a distribution before 5 min is also shown to highlight the initial formation of small particles (due to the slower coprecipitation of the pure NiOx, a PSD before 5 min was not collectable). The earliest PSD times were chosen as the earliest time where the CLD plot had clear peaks. From the PSD plots at different time points it is clear that following the initial formation of crystals, which was indicated by the very sharp peaks in the size range smaller than 10 um, the nucleated particles continued to grow. Especially for the MnOx and Mn3Ni1Ox particles, significant shifting of the peak positions were observed until 30 min after the coprecipitation was initiated. After 30 min the CLDs, and correspondingly the calculated PSDs, changed very little. Fig. 4 shows the SEM images of the particles collected from the three different coprecipitation systems after an hour of mixing, which was after the TM solution concentrations and FBRM counts had stabilized for all three systems (Figs. 1 and 2). The pure manganese particles and the blend particles both had a platelet morphology (Fig. 4a, c). We speculate that the two lengths associated with the plate morphology – the short plate thickness and larger plate length/width associated with the larger flat surface, resulted in the two peaks in the PSDs observed for these systems. The pure Ni system did not produce plate shape particles but also had two peaks in the PSD, however, in this case the second larger PSD peak was attributed to particle aggregates in the NiOx system. The NiOx particles were observed to have highly aggregated clumps in the SEM (Fig. 4b), and even though SEM sample preparation may have influenced the aggregation process the size of these aggregates were consistent with the PSD observations. From the SEM images, surface roughness can be clearly observed on the pure manganese and the blend precipitate particles whereas the surface of the NiOx particles were relatively smooth. This observation of the smooth NiOx particles provides one possibility to explain the preference of the nickel solute to continue nucleating rather than depositing on the crystal surface. In the NiOx precipitate system the energy barrier of two dimensional crystal growth on a perfect surface would be much larger than that from a defect or higher surface area substrate, and additional nucleation of NiOx particles may instead be preferred. The conclusion of the nucleation stage in the blend system likely reflects the reduced driving force towards nucleation due to the decreasing Ni^{2+} concentration, combined with the surface roughness of the blend particles promoting precipitation through particle growth. The particle surface roughness, which favors particle growth over nucleation, decreased the distance between sites of growth on the particles, analogous to the critical distance between dislocation sites in 2-D particle nucleation and growth studies needing to be greater than the critical particle size to facilitate the nucleation over growth [38].

The nucleation and particle growth mechanisms can also be deduced by studying the evolution of PSDs, as described by Eberl et al. [39]. In many crystallization processes, the crystallite PSD has been observed to follow a lognormal distribution, which can be explained by the Law of Proportionate Effect (LPE): $X_{j+1} = X_j + \varepsilon_j X_j$, stating that a particle's growth rate is determined by its size (X) plus the proportionality constant (ε) [39]. X_j is the particle size in an early time point and X_{j+1} is the particle size after a defined interval of particle growth. The proportionality constant is dependent on many system

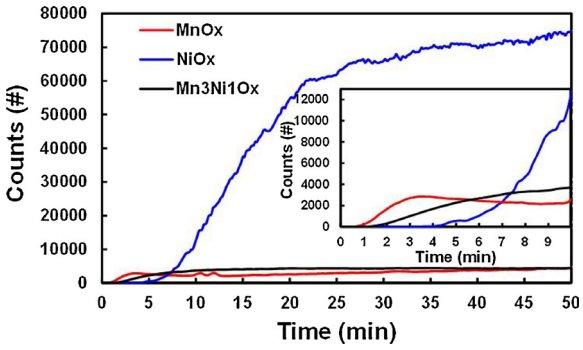

Fig. 2. FBRM total counts as a function of reaction time for pure nickel oxalate (NiOx, blue), pure manganese oxalate (MnOx, red), and manganese nickel blend oxalate (Mn3Ni1Ox, black) coprecipitation. Inset is an expanded view of the first 10 min. (For interpretation of the references to colour in this figure legend, the reader is referred to the web version of this article.)

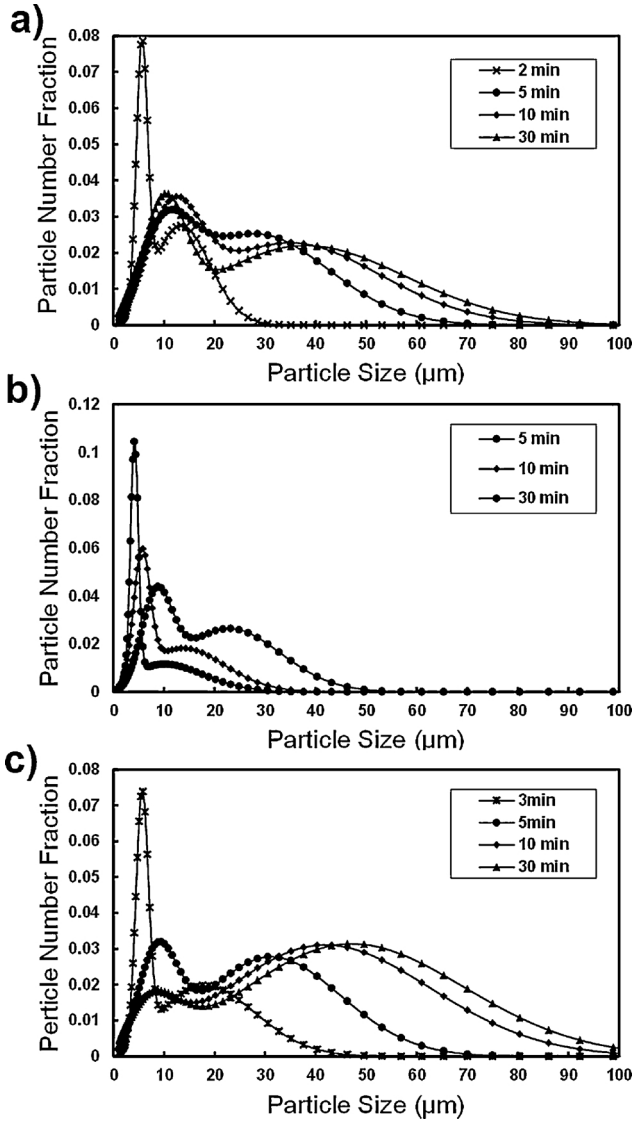

Fig. 3. Particle size distributions at 5, 10, and 30 min after the start of the precipitation in a) pure manganese oxalate (MnOx), b) pure nickel oxalate (NiOx), and c) manganese nickel blend oxalate (Mn3Ni1Ox). For a) and c), an earlier distribution is shown to highlight the initial formation of smaller particles in these faster precipitating systems. Solid lines added to guide the eye.

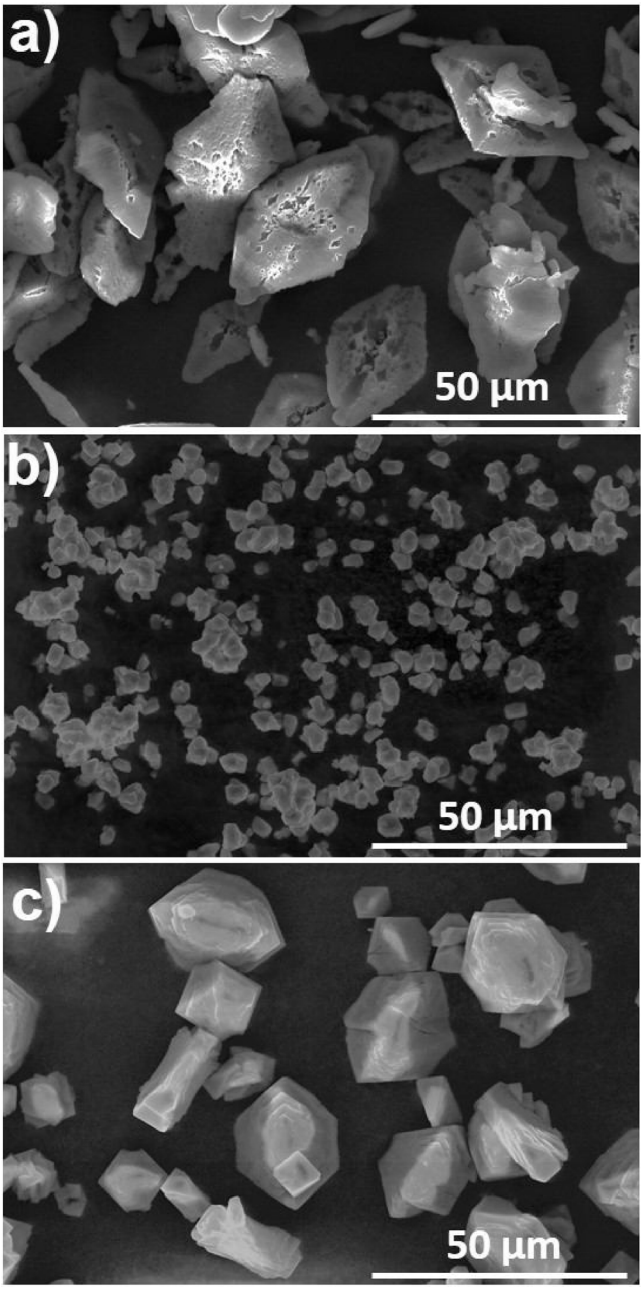

Fig. 4. SEM images of a) MnOx particles, b) NiOx particles, and c) Mn3Ni1Ox particles (from the 3:1 Mn:Ni blend feed coprecipitation reaction) collected after an hour of precipitating.

parameters, such as temperature and concentration. The lognormal distribution cannot fit well to the PSDs in the systems in this study due to either the particle size difference in different orientations (the platelet MnOx and Mn3Ni1Ox particles) or the segregation of tiny particles (NiOx particles). Thus, a fit with 2 log-normal distributions was used representing each of the PSD peaks. The obtained CLD data was also analyzed using the lognormal mean ($\alpha = \sum \ln(x) f(x)$) and variance ($\beta^2 = \sum [\ln(x) - \alpha]^2 f(x)$), and the results were compatible with applying the approach of Eberl at al. In that study, it was proposed that in addition to considering the entire shape of the PSD, growth mechanisms can be extracted from the evolution of β^2 with respect to α for a series of sample sets. In Fig. 5, β^2 are plotted on the y-axis with respect to α on the x-axis. Since α scaled with particle size, smaller α values correspond to earlier time points in the precipitation and increasing α values correlate with later times for all the precipitation systems. As shown in Fig. 5, at smaller values of α (earlier times in the reaction) β^2 had a linear dependence on α for the pure manganese which indicated a surface-controlled growth, whereas for the pure nickel precipitation β^2 had an exponential dependence on α indicating a continuous nucleation and growth mechanism [39]. The slope of the curve for NiOx in early stages of the coprecipitation was very gentle, indicating that the new particle nucleation occurred simultaneously during the growth of existing particles, but at a slow rate. The β^2 value dropped sharply after 30 min in NiOx coprecipitation, which could be due to Ostwald ripening where the smaller particles dissolved while the larger particles grow larger [39]. In contrast, the variance for the MnOx precipitates remained almost constant in the later stages (after 30 min) of the reaction, which followed well the pattern of a supply-controlled growth mechanism [39]. The variance of the PSD in Mn3Ni1Ox reaction also increased linearly with the lognormal mean and the slope was identical with that of the pure manganese precipitation. The intercepts of the lines, however, were different, which was due to the different initial PSDs before the growth phase was initiated. The nucleation reaction in MnOx coprecipitation ceased after the very short induction period and

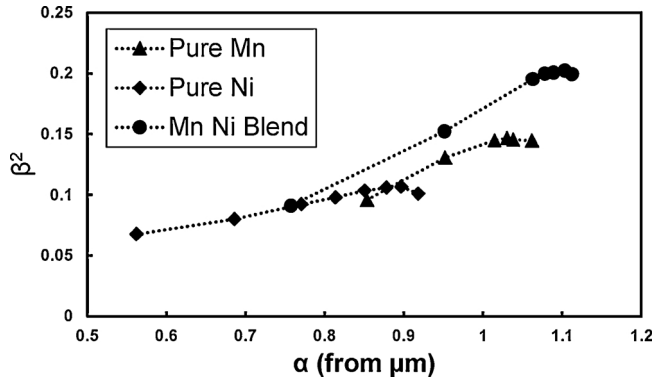

Fig. 5. The lognormal variation β^2 vs. lognormal mean α of the experimentally measured chord length distributions for the pure manganese precipitate (MnOx, triangles), pure nickel precipitate (NiOx, diamonds), and the blend precipitate (Mn3Ni1Ox, circles). Dashed lines added to guide the eye.

rendered the initial particles within a narrow size range, while in the blend precipitation the continuous nucleation of particles induced an asymptotic initial distribution. It can be seen from Fig. 5 that the initial starting point of the blend system was between measured values of the pure MnOx and NiOx precipitations. Other than the initial PSDs, the blend precipitation exhibited the same pattern and thus followed the same surface-controlled growth mechanism as the MnOx. This behaviour was also consistent with the similar consumed ion fractions and rates (Fig. 1d) for the MnOx and Mn3Ni1Ox systems. We speculate that the rough crystal surface lowered the energy barrier of nickel ions to deposit and grow on the crystal surface during the Mn3Ni1Ox coprecipitations and thus facilitated the precipitation of nickel ions in the blend system. At later times, the blend precipitation had a reduction in the rate of increase of β^2, which may have been due to both the ripening and supply-controlled growth mechanisms playing a role.

Using the measured concentrations of the TMs for the three systems (Fig. 1), the rate of the coprecipitation reaction was determined for each TM by numerically calculating the change in concentration divided by the change in time at each time point. The rate of the coprecipitation reaction was also normalized by the total surface area of particles that was available at that time for the TMs to deposit onto, and the particle surface was determined from the PSDs extracted from the FBRM measurements with the assumption that the particle sizes in the PSDs corresponded to spherical particles. Fig. 5 displays the logarithm of the TM coprecipitation rate plotted against the total TM concentration (or equivalently total oxalate, since the feed had the same concentration of both and the TM and oxalate precipitated at a 1:1 ratio). Starting with a rate expression of the form: $r = k[M]^{\delta}[Ox]^{\Theta}$, because the total TM and oxalate concentration were always equal in all three systems, the formula was simplified to $r = k[M]^{\gamma}$, of which the logarithm of both sides resulted in $\log r = \log k + \gamma log[M]$. A plot of log r as a function of log [M] thus had a slope which corresponded to the reaction order, and this plot for the three coprecipitation systems can be found in Fig. 6. As proposed by Doremus et al., there are two mechanisms of surface-controlled particle growth from ionic solute, either the ions form a molecule which is then adsorbed by the kinks of the particle surface ("molecule" mechanism) or the ions get adsorbed to the correct sites on the surface directly from the solution ("direct adsorption" mechanism) [40]. For the one-to-one electrolyte, as was the case for the TM oxalate coprecipitation in this study, the reaction rate would exhibit an order of three for the molecule mechanism and two for the direct adsorption mechanism. From linear fitting of the data from Fig. 6, the MnOx had a reaction order of 2.0, which fit well with the direct adsorption model. The NiOx precipitation, however, has a reaction order of 1.6. This deviation of reaction order below 2.0 may have been due to the simultaneous occurance of both nucleation and particle growth during the NiOx reaction, which consumed the solute in a relatively slower rate. The TM ion precipitation rate in the Mn3Ni1Ox system aligned well with the MnOx in the high concentration regime and with the NiOx in the low concentration regime. This result implies that the blend coprecipitation followed the same surface-controlled particle growth mechanism as in the MnOx in the early reaction period when the solute was adequate, and that it switched to the kinetics of NiOx precipitation as the reaction proceeded and less solute was residual in the solution. The two points from the blend system which approach the pure nickel precipitation mechanism corresponded to the reaction after 12 min of mixing, and at this time the Mn^{2+} consumption had almost plateaud and Ni^{2+}nickel was still significantly participating in the reaction. The decrease of critical particle size under the low supersaturation condition made the particle growth even on the rough particle surface more difficult and some of the precipitating Ni^{2+} may have switched back to the continuous nucleation mechanism [40]. This hypothesis of new particles nucleating in the Mn3Ni1Ox precipitation at later reaction times was supported by the slight increase of the small particle fraction in the PSDs (Fig. 2).

The growth mechanisms during precipitation of TM ions from pure and blend TM solutions provides fundamental knowledge necessary for rational battery material design and control, in the case where precipitate precursors are used for the production of battery active materials. Ideally, multicomponent precipitates would have controllable composition and particle size throughout a precipitation reaction process. Such control is important because of the sensitivity of the final materials processed using the TM precipitates with regards to composition and particle size on final material and electrochemical properties [5,41]. While determining an exact ideal size or morphology for a battery particle is challenging because of the need to match materials to a specific application and because of the multiple tradeoffs with particle morphology (e.g., length scales of ion transport within the particles, electrode microstructure pore sizes, areal electrode loading, electrode mechanical and thermal processes), there has recently been more attention to the impacts of heterogeneity and the lack of control of particle morphology and microstructure within the electrode [42]. Such heterogeneity can lead to uneven distribution of electrochemical activity, which results in excessive ageing of a subset of the active material particles within the electrode, resulting in both an electrochemical performance challenge and possibly a safety issue. In addition, intentional heterogeneity can result in particle distributions in the electrode that are used for different purposes, such as a blend where some particles provide high energy and others facilitate high pulsing power [43]. Rational control of these more complex and multicomponent electrodes will require a more complete understanding of the nucleation and growth processes of precursor particles used in the synthesis of the active materials – and this study is a first step towards

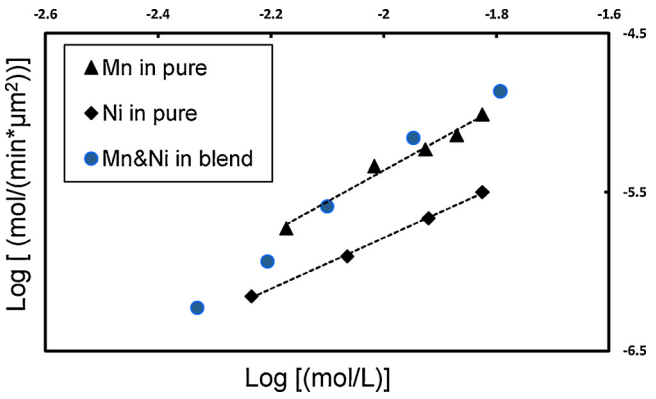

Fig. 6. Logarithms of the reaction rates as a function of the logarithms of the residual TM concentrations. Concentrations were for total TM, which was equivalent to oxalate concentrations in all experiments. Dashed lines represent from linear fits.

demonstrating tools such as FBRM which have not previously been applied to understand battery precursor synthesis and the processes that influence final particle morphology.

This study's main focus was the nucleation and particle growth processes for TM precipitates, and in particular it was found that properties such as crystal size and surface roughness contributed to the observed precipitation rate. The detailed nucleation and growth processes also influence final material composition in multicomponent systems, including both the total composition and the distribution of TMs within the particles. A systematic study on the external factors that influence the nucleation and particle growth process, such as feed concentration and solution temperature, will be needed to provide a more complete understanding of the nucleation and growth processes of the particles [19]. For these future systematic studies the population balance model can be applied to extract more quantitative information of the crystallization process in terms of the rate constants of nucleation, crystal growth, and aggregation [44–46].

4. Conclusion

In this work, in-situ FBRM measurements converted to PSDs were combined with ICP-OES measurements of solution compositional changes in-situ to track coprecipitation reaction processes as a function of time. Such information is necessary to understand the detailed nucleation and growth processes occurring in the solution, as well as to normalize the reaction rates for the coprecipitation. The FBRM provided insights into the timescales of particle nucleation and growth for variations in transition metal composition during oxalate coprecipitation. By comparison of the observations for pure nickel and manganese coprecipitation relative to coprecipitation of a blend of these transition metals, insights were gained into the mechanism by which nickel was consumed in a higher rate in a precipitation with a blend of Mn as opposed to precipitation in the absence of manganese ions. The experimental results demonstrated that the pure manganese and pure nickel precipitations followed different nucleation and particle growth paths. In the pure manganese oxalate precipitation, the nucleation ceases when the particle growth starts, which resulted in the solute being consumed at a faster rate. However, in the pure nickel oxalate precipitation, particle nucleation continues concurrent with the slower particle growth process, which resulted in a relatively slower observed reaction rate. In the blend system of manganese and nickel, rough particle surfaces helped to facilitate fast deposition of both transition metal ions on the surface; furthermore, manganese and nickel ions both followed an efficient surface-controlled direct adsorbing mechanism of precipitation. These observations explained why in the blend system both transition metal ions were consumed quickly and in a similar ratio, which resulted in a homogeneous blend precipitate, which would be desirable from a battery precursor synthesis standpoint. This study demonstrates the importance of understanding the nucleation and growth processes of precipitate particles when being used as precursors for multicomponent transition metal functional materials such as metal oxides. The different nucleation and growth mechanisms influence the composition of the final precipitates, the size and size distribution of the collected particles, and the timescale of the precipitation process. All of these outcomes are very important to resulting material properties and for rational predictive design of particulate reactors for making these materials.

Acknowledgements

This work was funded by the National Science Foundation, through grant awards CBET-1652488 and ECCS-1405134. The authors also thank Prof. Geoff Geise for use of their lab's TGA instrument.

References

[1] J.B. Goodenough, K.-S.S. Park, The li-ion rechargeable battery: a perspective, J. Am. Chem. Soc. 135 (2013) 1167–1176, https://doi.org/10.1021/ja3091438.
[2] N. Nitta, F. Wu, J.T. Lee, G. Yushin, Li-ion battery materials: present and future, Mater. Today 18 (2015) 252–264, https://doi.org/10.1016/j.mattod.2014.10.040.
[3] J.M. Tarascon, M. Armand, Issues and challenges facing rechargeable lithium batteries, Nature 414 (2001) 359–367, https://doi.org/10.1038/35104644.
[4] E. Vinodkumar, R. Marom, R. Elazari, G. Salitra, D. Aurbach, Challenges in the development of advanced Li-ion batteries: a review, Energy Environ. Sci. 4 (2011) 3243–3262, https://doi.org/10.1039/c1ee01598b.
[5] H. Dong, G.M. Koenig Jr, Compositional control of precipitate precursors for lithium-ion battery active materials: role of solution equilibrium and precipitation rate, J. Mater. Chem. A 5 (2017) 13785–13798, https://doi.org/10.1039/C7TA03653A.
[6] M.M. Thackeray, S.-H. Kang, C.S. Johnson, J.T. Vaughey, R. Benedek, S.A. Hackney, Li2MnO3-stabilized LiMO2 (M = Mn, Ni, Co) electrodes for lithium-ion batteries, J. Mater. Chem. 17 (2007) 3112–3125, https://doi.org/10.1039/B702425H.
[7] C.S. Johnson, N. Li, C. Lefief, J.T. Vaughey, M.M. Thackeray, Synthesis, characterization and electrochemistry of lithium battery electrodes: xLi2MnO3·(1 − x) LiMn0.333Ni0.333Co0.333O2 (0 ≤ x ≤ 0.7), Chem. Mater. 20 (2008) 6095–6106, https://doi.org/10.1021/cm801245r.
[8] L. Wan, Y. Deng, C. Yang, H. Xu, X. Qin, G. Chen, Ni/Mn ratio and morphology-dependent crystallographic facet structure and electrochemical properties of the high-voltage spinel LiNi0.5Mn1.5O4 cathode material, RSC Adv. 5 (2015) 25988–25997, https://doi.org/10.1039/C5RA03602J.
[9] H. Duncan, B. Hai, M. Leskes, C.P. Grey, G. Chen, Relationships between Mn 3 + content, structural ordering, phase transformation, and kinetic properties in lini x mn 2– x o 4 cathode materials, Chem. Mater. 26 (2014) 5374–5382, https://doi.org/10.1021/cm502607v.
[10] K.R. Chemelewski, D.W. Shin, W. Li, A. Manthiram, Octahedral and truncated high-voltage spinel cathodes: the role of morphology and surface planes in electrochemical properties, J. Mater. Chem. A 1 (2013) 3347, https://doi.org/10.1039/c3ta00682d.
[11] H. Dong, A. Wang, G.M. Koenig, Role of coprecipitation and calcination of precursors on phase homogeneity and electrochemical properties of battery active materials, Powder Technol. 335 (2018), https://doi.org/10.1016/j.powtec.2018.05.020.
[12] D. Wang, I. Belharouak, L.H. Ortega, X. Zhang, R. Xu, D. Zhou, G. Zhou, K. Amine, Synthesis of high capacity cathodes for lithium-ion batteries by morphology-tailored hydroxide co-precipitation, J. Power Sources 274 (2015) 451–457, https://doi.org/10.1016/j.jpowsour.2014.10.016.
[13] L. Li, X. Zhang, R. Chen, T. Zhao, J. Lu, F. Wu, K. Amine, Synthesis and electrochemical performance of cathode material Li1.2Co0.13Ni0.13Mn0.54O2 from spent lithium-ion batteries, J. Power Sources 249 (2014) 28–34, https://doi.org/10.1016/j.jpowsour.2013.10.092.
[14] L. Yang, G. Xi, Preparation and electrochemical performance of LiNi1/3Co1/3Mn1/3O2 cathode materials for lithium-ion batteries from spent mixed alkaline batteries, J. Electron. Mater. 45 (2015) 301–306, https://doi.org/10.1007/s11664-015-4067-z.
[15] H. Liu, L. Tan, High rate performance of novel cathode material Li1.33Ni1/3Co1/3Mn1/3O2 for lithium ion batteries, Mater. Chem. Phys. 129 (2011) 729–732, https://doi.org/10.1016/j.matchemphys.2011.04.031.
[16] X. Zhang, F. Cheng, K. Zhang, Y. Liang, S. Yang, J. Liang, J. Chen, Facile polymer-assisted synthesis of LiNi0.5Mn1.5O4 with a hierarchical micro–nano structure and high rate capability, RSC Adv. 2 (2012) 5669, https://doi.org/10.1039/c2ra20669b.
[17] S. Wu, C.W. Yang, Preparation of LiNi0.8Co0.2O2-based cathode materials for lithium batteries by a co-precipitation method, J. Power Sources 146 (2005) 270–274, https://doi.org/10.1016/j.jpowsour.2005.03.027.
[18] P. Axmann, G. Gabrielli, M. Wohlfahrt-Mehrens, Tailoring high-voltage and high-performance LiNi0.5Mn1.5O4 cathode material for high energy lithium-ion batteries, J. Power Sources 301 (2016) 151–159, https://doi.org/10.1016/j.jpowsour.2015.10.010.
[19] J.P. Robinson, G.M. Koenig, Tuning solution chemistry for morphology control of lithium-ion battery precursor particles, Powder Technol. 284 (2015) 225–230, https://doi.org/10.1016/j.powtec.2015.06.070.
[20] D. Sarkar, X.-T. Doan, Z. Ying, R. Srinivasan, In situ particle size estimation for crystallization processes by multivariate image analysis, Chem. Eng. Sci. 64 (2009) 9–19, https://doi.org/10.1016/J.CES.2008.09.007.
[21] J. Eggers, M. Kempkes, M. Mazzotti, Measurement of size and shape distributions of particles through image analysis, Chem. Eng. Sci. 63 (2008) 5513–5521, https://doi.org/10.1016/J.CES.2008.08.007.
[22] B. Presles, J. Debayle, G. Fevotte, J.-C. Pinoli, Novel image analysis method for *in situ* monitoring the particle size distribution of batch crystallization processes, J. Electron. Imaging 19 (2010) 031207, , https://doi.org/10.1117/1.3462800.
[23] J. Calderon De Anda, X.Z. Wang, X. Lai, K.J. Roberts, Classifying organic crystals via in-process image analysis and the use of monitoring charts to follow polymorphic and morphological changes, J. Process Control 15 (2005) 785–797, https://doi.org/10.1016/J.JPROCONT.2005.02.002.
[24] S.-Y. Yoon, Y. Deng, Flocculation and reflocculation of clay suspension by different polymer systems under turbulent conditions, J. Colloid Interface Sci. 278 (2004) 139–145, https://doi.org/10.1016/J.JCIS.2004.05.011.
[25] J.C. Alfano, P.W. Carter, A.J. Dunham, M.J. Nowak, K.R. Tubergen, Polyelectrolyte-induced aggregation of microcrystalline cellulose: reversibility and shear effects, J.

Colloid Interface Sci. 223 (2000) 244–254, https://doi.org/10.1006/JCIS.1999.6651.
[26] P. Raj, W. Batchelor, A. Blanco, E. de la Fuente, C. Negro, G. Garnier, Effect of polyelectrolyte morphology and adsorption on the mechanism of nanocellulose flocculation, J. Colloid Interface Sci. 481 (2016) 158–167, https://doi.org/10.1016/j.jcis.2016.07.048.
[27] N. Doki, H. Seki, K. Takano, H. Asatani, M. Yokota, N. Kubota, Process control of seeded batch cooling crystallization of the metastable α-form glycine using an in-situ ATR-FTIR spectrometer and an in-situ FBRM particle counter, Cryst. Growth Des. 4 (2004) 949–953, https://doi.org/10.1021/cg030070s.
[28] Z.Q. Yu, P.S. Chow, R.B.H. Tan, Interpretation of focused beam reflectance measurement (FBRM) data via simulated crystallization, Org. Process Res. Dev. 12 (2008) 646–654, https://doi.org/10.1021/op800063n.
[29] B. De Clercq, P.A. Lant, P.A. Vanrolleghem, Focused beam reflectance technique for in situ particle sizing in wastewater treatment settling tanks, J. Chem. Technol. Biotechnol. 79 (2004) 610–618, https://doi.org/10.1002/jctb.1028.
[30] A.V. Pandit, V.R. Vivek, Chord length distribution to particle size distribution, AIChE J. 62 (2016) 4215–4228, https://doi.org/10.1002/aic.
[31] E. Zhao, M. Chen, D. Chen, X. Xiao, Z. Hu, A versatile coating strategy to highly improve the electrochemical properties of layered oxide LiMO2(M = Ni0.5Mn0.5and Ni1/3Mn1/3Co1/3), ACS Appl. Mater. Interfaces 7 (2015) 27096–27105, https://doi.org/10.1021/acsami.5b08777.
[32] F. Wu, H. Lu, Y. Su, N. Li, L. Bao, S. Chen, Preparation and electrochemical performance of Li-rich layered cathode material, Li[Ni0.2Li0.2Mn0.6]O2, for lithium-ion batteries, J. Appl. Electrochem. 40 (2010) 783–789, https://doi.org/10.1007/s10800-009-0057-2.
[33] A. Manthiram, K. Chemelewski, E.-S. Lee, A perspective on the high-voltage LiMn1.5Ni0.5O4 spinel cathode for lithium-ion batteries, Energy Environ. Sci. 7 (2014) 1339, https://doi.org/10.1039/c3ee42981d.
[34] R. Marom, S.F. Amalraj, N. Leifer, D. Jacob, D. Aurbach, A review of advanced and practical lithium battery materials, J. Mater. Chem. 21 (2011) 9938–9954, https://doi.org/10.1039/C0JM04225K.
[35] D. Wang, I. Belharouak, G.M. Koenig, G. Zhou, K. Amine, Growth mechanism of Ni0.3Mn0.7CO3 precursor for high capacity Li-ion battery cathodes, J. Mater. Chem. 21 (2011) 9290, https://doi.org/10.1039/c1jm11077b.
[36] Y.Y. Yang, S. Xu, M. Xie, Y. He, G. Huang, Y.Y. Yang, Growth mechanisms for spherical mixed hydroxide agglomerates prepared by co-precipitation method: a case of Ni1/3Co1/3Mn1/3(OH)2, J. Alloys Compd. 619 (2015) 846–853, https://doi.org/10.1016/j.jallcom.2014.08.152.
[37] M. Aoun, E. Plasari, R. David, J. Villermaux, A simultaneous determination of nucleation and growth rates from batch spontaneous precipitation, Chem. Eng. Sci. 54 (1999) 1161–1180, https://doi.org/10.1016/S0009-2509(98)00488-6.
[38] J.A. Dirksen, T.A. Ring, Fundamentals of crystallization: kinetic effects on particle size distributions and morphology, Chem. Eng. Sci. 46 (1991) 2389–2427, https://doi.org/10.1016/0009-2509(91)80035-W.
[39] D.D. Eberl, V.A. Drits, J. Środoń, Deducing growth mechanisms for minerals from the shapes of crystal size distributions, Am. J. Sci. 298 (1998) 499–533, https://doi.org/10.2475/ajs.298.6.499.
[40] R. Doremus, Precipitation kinetics of ionic salts from solution, J. Phys. Chem. (1968) 2158, https://doi.org/10.1021/j150567a011.
[41] Y. Xue, Z. Wang, L. Zheng, F. Yu, B. Liu, Y. Zhang, K. Ke, Investigation on preparation and performance of spinel LiNi0.5Mn1.5O4 with different microstructures for lithium-ion batteries, Sci. Rep. 5 (2015) 13299, https://doi.org/10.1038/srep13299.
[42] S.J. Harris, P. Lu, Effects of inhomogeneities -nanoscale to mesoscale -on the durability of Li-ion batteries, J. Phys. Chem. C. 117 (2013) 6481–6492, https://doi.org/10.1021/jp311431z.
[43] K.G. Gallagher, S.-H. Kang, S.U. Park, S.Y. Han, xLi2MnO3·(1 − x)LiMO2 blended with LiFePO4 to achieve high energy density and pulse power capability, J. Power Sources 196 (2011) 9702–9707, https://doi.org/10.1016/J.JPOWSOUR.2011.07.054.
[44] C.B.B. Costa, M.R.W. Maciel, R.M. Filho, Considerations on the crystallization modeling: population balance solution, Comput. Chem. Eng. 31 (2007) 206–218, https://doi.org/10.1016/J.COMPCHEMENG.2006.06.005.
[45] H.M. Omar, S. Rohani, Crystal population balance formulation and solution methods: a review, Cryst. Growth Des. 17 (2017) 4028–4041, https://doi.org/10.1021/acs.cgd.7b00645.
[46] Z.K. Nagy, A population balance model approach for crystallization product engineering via distribution shaping control, Comput. Aided Chem. Eng. 25 (2008) 139–144, https://doi.org/10.1016/S1570-7946(08)80028-4.